Automatic space object detection on all-sky images from a synoptic survey synthetic telescope array

Felipe I. San Martín [a], Claudio A. Perez [a,*], Juan E. Tapia [b], Shahzad Virani [c], Marcus J. Holzinger [c]

[a] *Department of Electrical Engineering and Advanced Mining Technology Center, Universidad de Chile, Av. Tupper 2007, Santiago 8370451, Chile*
[b] *Universidad Tecnologica de Chile – Inacap, Avenida del Condor 720, Santiago 8580704, Chile*
[c] *Ann and H.J. Smead Aerospace Engineering Sciences, University of Colorado, Boulder, 429 UCB University of Colorado Boulder 80309, USA*

Abstract

Detection, classification, and characterization of Space Objects (SOs) are important tasks in many areas of research. Detection of SOs is important in predicting collisions with debris that could become hazards for satellites or space missions in Near Earth orbits. This paper describes a flexible pipeline able to detect sunlit SOs automatically in images acquired using an all-sky camera with a large field of view (FoV). The proposed pipeline includes the following main steps: image distortion correction, filtering for noise reduction, generation of a background model for subtraction, star elimination using a star catalog, local-based contrast enhancement, and, finally, for automatic SO detection, two methodologies were developed to detect line segments. The first one uses a Canny edge detector and a Progressive Probabilistic Hough Transform, and the second is based on the Radon Transform for detecting line segments. The method was applied to a dataset of 22×3 images obtained from the Omnidirectional Space Situational Awareness (OmniSSA) Array at the Georgia Institute of Technology in downtown Atlanta. The OmniSSA array has 3 sensors that capture high-resolution images simultaneously (3352×2532 pixels) using a wide FoV for each camera. An intensity scaled by noise (I_{SN}) signal was defined and measured to show improvement in SO detection objectively. Fusing images from the three OmniSSA sensors after the background subtraction step improved both the I_{SN} and visualization during the detection stage. Ground-truth data were extracted from a Space-Track catalog and marked by human experts to validate the results of the pipeline, considering information from Astrometry.net. Results showed that almost all the SOs were correctly detected by the pipeline.
© 2019 COSPAR. Published by Elsevier Ltd. All rights reserved.

Keywords: Space debris; Image processing; Automatic detection

1. Introduction

The study of Space Objects (SOs) is an active research field in which groups around the world have designed and built specialized hardware and algorithms for detection, classification, and characterization of these objects. This field is important because it can contribute to predicting collisions in space and to analyzing their consequences (Pardini and Anselmo, 2011). Space missions and satellites produce space debris that increases the probability of new mission failures due to impacts (Krag et al., 2017; Landgraf et al., 2004), making the detection of SOs very important (Klinkrad, 2010).

Since SOs move fast, they fall into the time-domain Astronomy category, with several differences with respect

to classical Astronomy, especially in terms of hardware because the field of view (FoV) and cadence requirements are distinct. Given these differences, new systems have been developed to search for SOs, including the following: Canadian Automated Meteor Observatory (CAMO) (Weryk et al., 2013), Spanish Meteor Network (SPMN) (Trigo-Rodriguez et al., 2008), Croatian Meteor Network (CMN) (Gural, 2008), TAROT (Laas-Bourez et al., 2009), Southern Ontario All-Sky Meteor Camera Network (Weryk et al., 2008) and OmniSSA (Grøtte et al., 2016).

In addition to the development of new specialized hardware, it is important to have methods that can process the acquired data and detect SOs efficiently. In this context, Torteeka et al. (2017) used a track-before-detect approach to detect transient objects. In another approach, Trigo-Rodriguez et al. (2008) developed the SPanish Fireball Network (SPFN), and captured images with 90 s of exposure time. The method compared two consecutive frames and applied a variant of the Hough Transform to detect SOs. Similarly, in Laas-Bourez et al. (2009) the researchers used a variant of the Hough Transform, but with single images. Zimmer et al. (2013) developed a strategy using a variant of the Radon Transform, and took advantage of dedicated hardware, a GPU, to run the algorithm faster. Matched filter strategies also have been developed (Murphy et al., 2016), and machine learning techniques to detect SOs have been applied as well (Virtanen et al., 2016).

In this paper, we present a flexible pipeline for automatic detection of SOs. The proposed method increases the Intensity Scaled by Noise (I_{SN}) measure in the processed images using image enhancement algorithms for later detection of SOs in the image sequences. The proposed pipeline includes the following main steps applied to the input image: image distortion correction, filtering for noise reduction, generation of a background model from data to subtract it from the filtered image, star elimination using a star catalog, and local-based contrast enhancement. The star elimination step using a star catalog to eliminate only the brighter stars for SOs detection was recently reported in Zimmer et al. (2018). A similar approach has been used for NEOs or by using frame differing, although in the latter all the information present in the image is subtracted instead of selectively brighter stars. Finally, two methodologies were developed for automatic SO detection. The first one uses a Canny edge detector and a Progressive Probabilistic Hough Transform segment detector. The second method is based on the Radon Transform to detect SOs. The proposed pipeline was tested using a dataset of images obtained from the Omnidirectional Space Situational Awareness (OmniSSA) Array dataset (Grøtte et al., 2016) and the ground-truth was marked using the Space-Track catalog. Since the OmniSSA has three sensors capturing three images simultaneously, an image fusion step was added to the pipeline after the background subtraction step. Results show that the proposed pipeline produces significant improvement in the processed

I_{SN} images, and can automatically detect almost all SOs in the marked ground-truth dataset.

2. Methods

The proposed method consists of several steps that are divided into two main stages: image enhancement, and automatic SO detection. The image enhancement pipeline includes the following steps: correction of image distortion, median filtering for noise reduction, generation of a background model to be subtracted from the filtered image, image fusion using data from the three OmniSSA sensors, star removal using a star catalog, and enhancement of local-zone contrast. Two alternative approaches were developed for the Automatic SO Detection stage. The first uses a Canny edge detector and a Progressive Probabilistic Hough Transform segment indicator, and the second one makes use of the Radon Transform for SOs detection.

2.1. Image enhancement

2.1.1. Correction of image distortion
Camera lenses generate a geometric distortion of the captured images, which can be corrected using camera calibration parameters (Grøtte et al., 2016). We use the distortion proposed by Fryer and Brown (1986), which considers radial and tangential distortion. This model is given by

$$\begin{bmatrix} x_d \\ y_d \end{bmatrix} = \begin{bmatrix} x_u \\ y_u \end{bmatrix} + \begin{bmatrix} x_u r^2 & x_u r^4 & x_u r^6 & 2x_u y_u & r_2 + 2x_u^2 \\ y_u r^2 & y_u r^4 & y_u r^6 & r^2 + 2y_u^2 & 2x_u y_u \end{bmatrix} \begin{bmatrix} K_1 \\ K_2 \\ K_3 \\ P_1 \\ P_2 \end{bmatrix}$$

(1)

$$r^2 = x_u^2 + y_u^2 \tag{2}$$

where $(\cdot)_d$ are the distorted coordinates, $(\cdot)_u$ are the undistorted coordinates, $K1, K2, K3$ are the radial distortion parameters and $P1, P2$ are the tangential distortion parameters. This step is commonly used in computer vision tasks, and is crucial in this problem for the astrometric calibration making a comparison of the processed image with the corresponding image of the star catalog possible.

For the same sensors, a distortion analysis and image distortion correction was performed by Grøtte et al. (2016). We used their results to develop our system.

2.1.2. Median filtering
With the purpose of eliminating extreme-valued noise from the captured images, a 3×3 spatial median filter (Huang et al., 1979) is applied to each image. The median is computed for each window of 3×3 pixels in every pixel of the image. The median filter is widely used in image processing and astronomy (Mellinger, 2009) to reduce artifacts, including hot pixels, and noise that is characterized as salt-and-pepper noise.

2.1.3. Background subtraction

Using the filtered images from Section 2.1.2., a background model was generated by computing the median image from the dataset images (Cheung and Kamath, 2005; Cucchiara et al., 2003). To compute the background model, a temporal median filter was applied using the median value for each pixel of the stack. In this case the stack is composed of 22 images and therefore the median of 22 pixels is computed for each pixel of the image. Next, the background model was subtracted from each filtered image. Background subtraction is generally used to improve photometry and detection (Blanton et al., 2011) by eliminating both the CCD noise, and that provoked by the lighting conditions on the lens. In our particular case, the large field of view causes substantial distortion, meaning that pixels in the center of the field of view have a different amount of background light than those close to the edges. Hot pixels, that may persist after applying the median filter, are also removed by background subtraction.

2.1.4. Image fusion

Because the OmniSSA array captures three images simultaneously, it is possible to fuse them to generate an image with reduced noise. To do so, it is necessary to register the three images using the brighter stars as references. The registration among the three images was performed using the 100 most brilliant stars, and a Projective Transform was used to correct deformations (Hartley and Zisserman, 2003). Since the three cameras keep their position fixed, the transform is computed only once, and the same transform is useful to all captures. We apply a projective transform to rectified images, thus we expect that all images have the same higher order distortion coefficients. Grøtte et al. (2016) made a detailed description of the hardware used to develop the OmniSSA device, which has three identical cameras and lenses. The temperature change in the CCD between the first and last capture is less than 0.71°C. Therefore, we considered the sensor and lens parameters constant during the capture time (Podbreznik and Potočnik, 2012).

2.1.5. Star removal

For the problem of SO detection, stars impede proper contrast stretching because of their natural high brightness. Therefore, most bright stars were removed from the image sequence. To accomplish the star removal, bright areas were detected in each image and compared to the same area of the Tycho-2 star catalog using the Astrometry.net software (Lang et al., 2010). The pixels corresponding to the stars were replaced by the median value of a neighborhood surrounding each star. Astrometry.net also finds the inertial right-ascension and declination coordinates in which each image is located. Considering the size of the most bright stars that were candidates to be removed, a fixed circle with radius of 10 pixels was used as star excision neighborhood. The process of star removal is crucial because it allows targeting the contrast enhancement on the rest of the gray levels, once the bright stars are removed.

2.1.6. Image division into zones

Contrast enhancement needs to be performed adapted to different zones of the image because the field of view of all-sky cameras is wide, and image brightness varies significantly from one zone to another. The image brightness has significant variations across the FOV because of celestial bodies such as the North America Nebula that appear at varying spatial positions in different frames. Therefore, these sources of brightness are not eliminated by background subtraction. As the FOV is very wide, there are significant differences in brightness among various zones. To enhance contrast locally, the image was divided into zones. Edges were detected in each zone, but an overlap of 20% among neighboring zones was allowed to avoid detecting artificial edges around zone boundaries while applying the edge detector.

2.1.7. Adaptive contrast enhancement for zones

Contrast enhancement changes the pixel value distribution to cover a wider range. Adaptive contrast enhancement allows adjusting changes in the pixel value distribution to the local brightness of the image in different zones. Contrast enhancement is required to separate SOs from the background as has been described in many applications with low contrast (Xie and Lam, 2006; Perez et al., 2010; Cament et al., 2015). For this purpose, a contrast stretching method was used (Lim, 1990), which was applied locally to each zone producing a saturation of dark and bright pixels between 1% and 97% of the image brightness. In this way, contrast stretching was adapted to the content of the image in the different zones.

Contrast stretching methods are useful for improving the results of the image processing algorithms, especially when involves a non-linear transformation in the distribution of pixel values (Xie and Lam, 2006; Castillo et al., 2014). Illumination compensation has proven to be crucial in many machine vision applications including object detection, and face recognition (Perez et al., 2010; Cament et al., 2015; Perez et al., 2011). This is especially important in non-controlled scenarios where illumination is not homogeneous and algorithms for line detection, such as Canny edge detection, Progressive Probabilistic Hough Transform and Radon Transform, are being applied (Xie and Lam, 2006; Perez et al., 2010; Cament et al., 2014). In our present paper, because the extreme values in the images are saturated, we use a non-linear transformation. Additionally, with our data no object detection is obtained if the contrast stretching is not performed previous to Canny edge detection, Progressive Probabilistic Hough Transform and Radon Transform. Figure 8 shows the

results of the edge detection step if no contrast stretching is applied previously for the Canny edge detection method.

2.2. Automatic space object detection stage

2.2.1. Edge and streak detector based on the Hough transform

A moving object is observed as a line segment (streak) in captured images from a synoptic survey telescope. A Canny edge detector (Canny, 1986) was used to find these line segments through a procedure applied to each zone to avoid detecting artificial edges generated along neighboring zones (Cament et al., 2014, 2015; Tapia et al., 2016). After applying the Canny Edge Detector, we obtain a binary image from each zone of the image. As there is an overlap between adjacent zones, it is necessary to merge detections. Thus, we apply an OR operator among detections from different zones.

Since SOs are observed as line segments in the images, a Progressive Probabilistic Hough Transform Segment Detector (Galamhos et al., 1999; Cament et al., 2015; Castillo et al., 2014) was applied after the Canny edge detector. This transform is widely used to detect objects with known geometry.

2.2.2. Radon transform for streak detection

An alternative method was implemented to detect streaks (line segments) based on the Radon Transform (Radon, 1986; Zimmer et al., 2013). This transform is similar to the Hough Transform, but uses the real value of each pixel without having to binarize the input image, thus allowing the detection of fainter streaks. The Radon Transform was applied in each zone of the image using the same zones defined for the adaptive contrast enhancement. Then, the local peaks were found in the parameter space (sinogram), and the streaks were detected by applying the Inverse Radon Transform to those peaks with values greater than a threshold. The threshold was automatically chosen as the sinogram mean plus three times its standard deviation. An overlap of 50% among neighboring zones was also allowed to generate redundant detections to facilitate the elimination of false positives generated by noise.

To validate our method, the Radon transform was implemented using Python 3 on an Intel (R) Core (TM) i7-7700 3.6 GHz, with 64 GB RAM. The computational time for one image was 163.47 s. However, this time could be reduced significantly by using C++ and a GPU implementation, as was shown by Zimmer et al. (2013).

2.3. Omnidirectional Space Situational Awareness (OmniSSA) Array dataset

The proposed method was evaluated on a dataset obtained from the OmniSSA Array at the Georgia Institute of Technology (Grøtte et al., 2016). Using the OmniSSA Array dataset, synoptic survey imaging activities with an ultra wide FoV could be investigated. Three simultaneously captured wide FoV images are available to improve both detection (photometric) and angular measurement (astrometric) properties. The OmniSSA array has three sensors equipped with a Rokinon 10 mm F/2.8 ED AS IF NCS lens, an SBIG FW5-8300 5-position filter wheel, and an SBIG STF-8300 M CCD that can take high-resolution images (3352×2532 pixels) with a bit-depth of 16 bits. It also has a wide FoV of $66° \times 82°$ for each camera.

The dataset is composed of 22 images captured by each sensor, 66 images in total, with an exposure time of 30 s. These images were taken on August 30, 2016 between 01:11:05 UT and 02:32:34 UT. The OmniSSA was the one located at Georgia Tech in downtown Atlanta, specifically at 33.777468° N, 84.398969° W.

All images used in this research have an exposure time of 30 s. The star trailing is approximately 6 pixels, considering both the FOV and exposure time. The largest star diameter is approximately 14 pixels. Therefore, the star excision of 20 pixels in diameter assures that the star trailing does not produce a problem. The OmniSSA has three sensors located at a distance of less than 50 cm among them, in a triangular arrangement as described in Grøtte et al. (2016).

2.4. Evaluation metric

2.4.1. Image enhancement

To evaluate image enhancement, the Intensity Scaled by Noise (I_{SN}) measure was defined as

$$I_{SN} = \frac{S}{\sigma_n} \tag{3}$$

where S is the intensity of a group of pixels and σ_n is the standard deviation of noise, since there are only few objects relative to the background, $\sigma_n = \sigma$ where σ is the standard deviation of the whole image.

We measure the mean of the standard deviation for each zone in an image as 0.0159 without contrast stretching. After applying contrast stretching, this value was reduced to 0.0012. Therefore, it is sufficiently small to assume a uniform standard deviation across the focal plane.

This definition makes direct comparisons among I_{SN} measures from images at various stages of the pipeline difficult since they have very different means and STDs. Therefore, we use the $I_{SN} - \overline{I_{SN}}$ to compare I_{SN} measures from different stages of the pipeline, where $\overline{I_{SN}}$ is the mean of the I_{SN}.

We use Eq. (3) to compare results at various processing steps. By selecting a group of rows of pixels, e.g., five rows in an image, the I_{SN} can be computed and plotted. It is
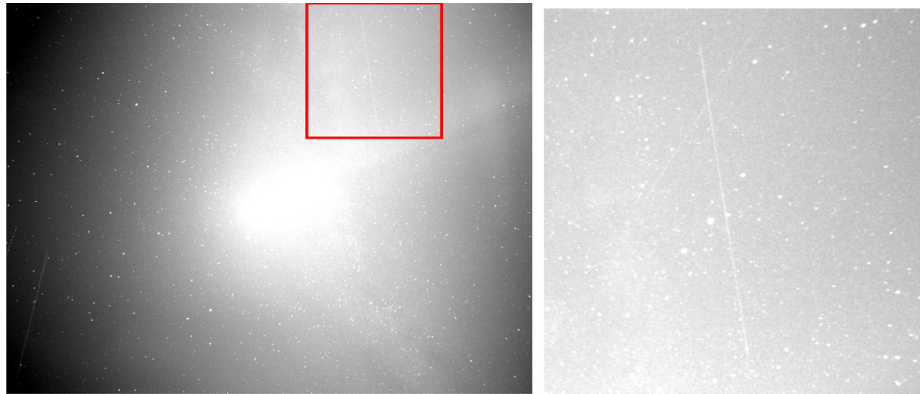
Fig. 1. Image Using an example to show results. (Left) Original Image with contrast stretching, (Right) Zoom of the image in the area marked in red. (For interpretation of the references to colour in this figure legend, the reader is referred to the web version of this article.)

expected that I_{SN} will peak while computing pixels that belong to SOs.

2.4.2. Detection stage

Information extracted from Space-Track Database[1] was used to determine the ground-truth for evaluating the accuracy of the proposed methods detection capacity. However, due to the hardware employed, and environment limitations, the OmniSSA array reached only a few hundred kilometers of depth into space (the atmosphere). Therefore, only SOs within this range are visible in the images. A total of 16 SOs were identified and marked on the ground-truth. In addition, there are some streaks on the images that were identified as airplanes, and are not counted as correct SOs detections. Using the defined ground-truth, Precision, Recall and f-score measurements can be calculated (Olson and Delen, 2008).

3. Experimental results

In the following sections, the results of the main steps from the proposed pipeline are presented. A cross-validation protocol (Geisser, 2017) was used to adjust the system's hyperparameters, using each image with presence of SOs, generating 9 folds in total. The test set was defined as another 21 captures. Therefore, in each fold, a single capture was used to train, and the remaining 21 captures were used to test the pipeline. The pipeline has several parameters that must be adjusted. For this purpose, we used a cross-validation procedure. Each parameter was adjusted using a single image (training) and the results were evaluated in the remaining set (test). Then, the single image was changed for another one and the adjustment/test procedure was repeated. Cross validation is widely used in machine learning, neural networks and image processing. To show a qualitative analysis, an image was used as an example. This image is shown in Fig. 1 and a zone of interest was marked by a rectangle. After that, the I_{SN} and the

$I_{SN} - \overline{I_{SN}}$ are plotted to compare improvements. Finally, the automatic SO detection is analyzed using Precision, Recall and f-score measurements.

3.1. Image enhancement

3.1.1. Background subtraction

The background model for each of the three sensors of the OmniSSA dataset images was obtained and is shown in Fig. 2 for sensor 1. The background was subtracted from each image. After this background subtraction, the mean for all images was reduced from 12652.93 to 50.73, and the standard deviation was reduced by a factor of 3.78, from 1151.49 to 304.12 on average. Fig. 3 shows the results of background subtraction applied to the example image. It can be observed that the contrast improved significantly after background subtraction, making objects, such as stars, more visible.

3.1.2. Image fusion

Through a geometric transformation found among the three cameras, an image stack was generated for each capture time. The geometric transformation is a projective transformation that allows us to align the images captured simultaneously. A fused image was obtained by adding the images from the three sensors. Fig. 4 shows the fused image from the three sensors.

3.1.3. Star removal

After executing the process for image fusion, further reduction in the standard deviation of brightness was introduced because many bright stars appeared as outliers on the background, and thus prevented further contrast stretching to enhance SOs trajectories. Fig. 5 shows the fused image with stars removed. The improvement in visualization is worth noting.

3.1.4. Contrast enhancement

Contrast stretching allows better viewing of SOs as shown in Fig. 6, but the enhancement is not optimal due

Fig. 2. Background model generated from the set of 23 OmniSSA images from sensor 1.

to pixels with high level intensity in the image. In Fig. 6 contrast stretching also enhances the presence of the North America Nebula, which may interfere with detecting possible SOs in that area of space.

3.1.5. Zone division for adaptive contrast stretching

Fig. 7 shows that contrast stretching adapted to each zone of the image improves the contrast enhancement. This improvement can be seen when Fig. 7 is compared to Fig. 6 in which contrast stretching was applied directly to the original image. Fig. 7 shows that contrast stretching adapted to different zones of the sky yields improved results in terms of SO detection, especially by the greater contrast among SOs and backgrounds. In this case, contrast enhancement is better within the area of the North America Nebula compared to the contrast of the detected SOs.

Contrast stretching algorithms improve the results of other image processing algorithms applied afterwards in cascade. The results of our pipeline without the contrast stretching step, increases the false alarm rate significantly. In Fig. 8 we show that the Canny Edge Detector applied directly without contrast stretching, does not detect any of the SO edges. The Canny Edge Detector first step is a Gaussian smoothing which virtually erases all SOs since their contrast is small. Therefore, SOs should be previously
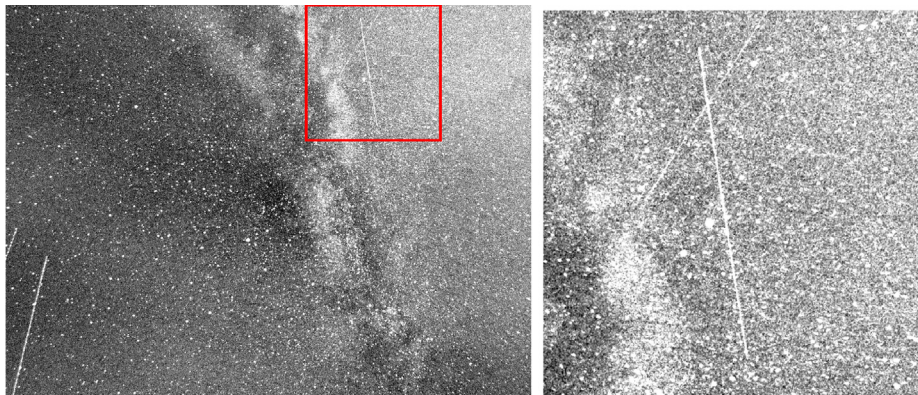

Fig. 3. Result of background subtraction on one image from the dataset. (Left) Image with background subtraction with improved contrast, (Right) Zoomed image in the area marked in red. (For interpretation of the references to colour in this figure legend, the reader is referred to the web version of this article.)
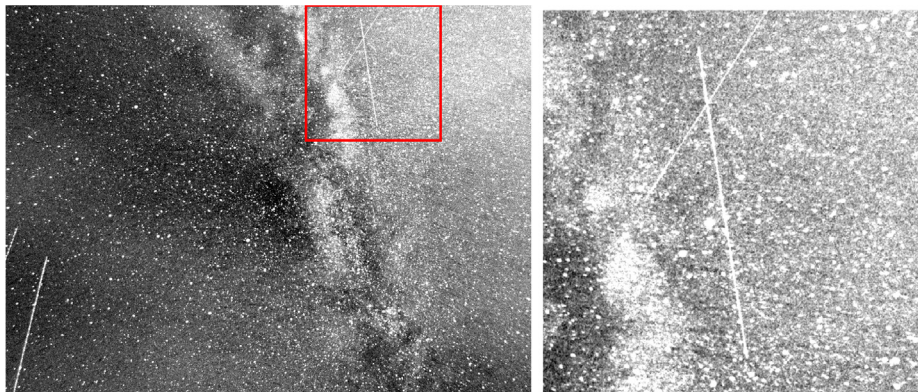

Fig. 4. (Left) Fused image by adding the images from the three sensors, (Right) Zoomed Image in the area marked in red. (For interpretation of the references to colour in this figure legend, the reader is referred to the web version of this article.)
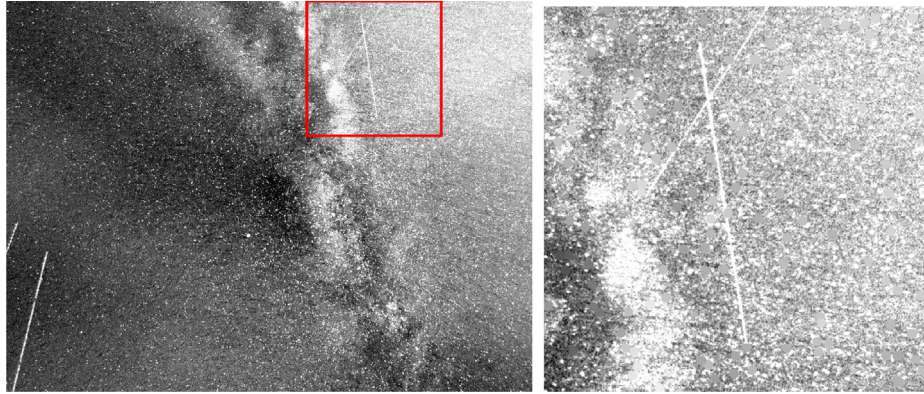
Fig. 5. (Left) Fused image with stars removed using results from Astrometry.net as the reference for star location, (Right) Zoomed Image in the area marked in red. (For interpretation of the references to colour in this figure legend, the reader is referred to the web version of this article.)
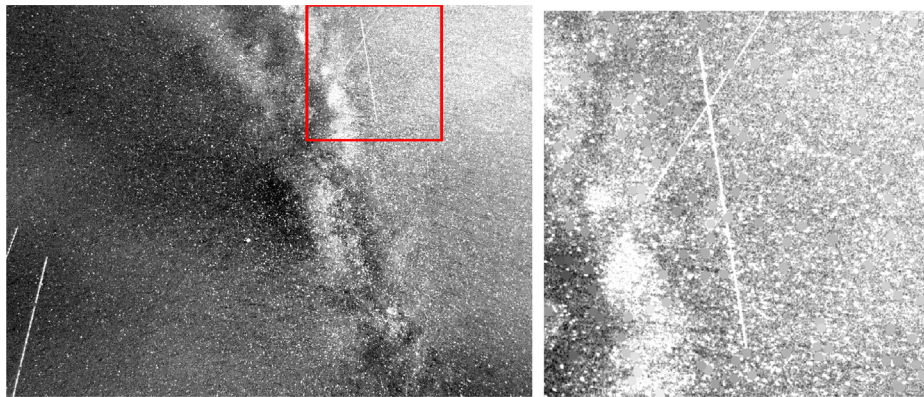

Fig. 6. (Left) Contrast Stretching on fused image with stars removed, (Right) Zoomed Image in the area marked in red. (For interpretation of the references to colour in this figure legend, the reader is referred to the web version of this article.)
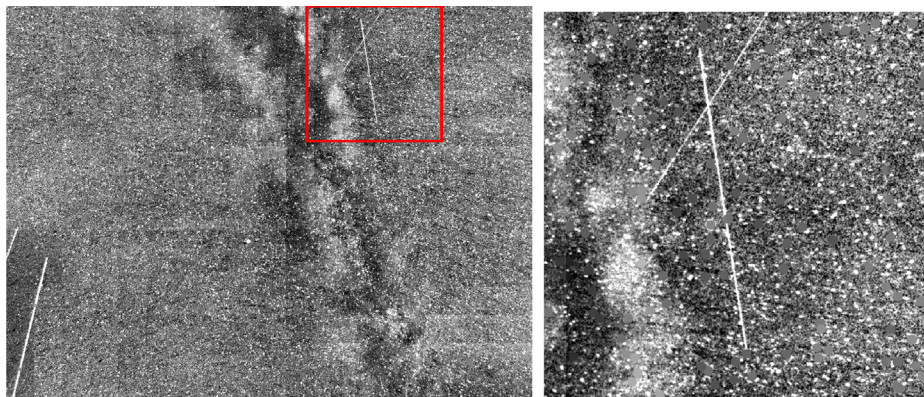

Fig. 7. (Left) Contrast Stretching applied to various zones, (Right) Zoomed Image in the area marked in red. (For interpretation of the references to colour in this figure legend, the reader is referred to the web version of this article.)

contrast enhanced before applying Canny Edge Detector. Fig. 8 shows the edge detection with no contrast stretching, where only the most brilliant stars could be detected.

3.1.6. I_{SN} measurement

The lower left section of Fig. 9 shows a group of five rows within the image, randomly chosen within the zone of detected SOs, in which the I_{SN} was measured using Eq. 3. These rows intersect two SOs in the image as is shown in the lower left part of Fig. 9 which is a zoom of the upper right part of Fig. 7. At the top-right of Fig. 9 the I_{SN} is plotted along the chosen rows showing the first peak between 8 and 15 pixels, and a second one, that is more diffuse, between 35 and 40 pixels. The I_{SN} was computed for different combinations of background subtraction (BS), image fusion (FU), star removal (SR), contrast stretching (CS),

Fig. 8. Results of applying Canny Edge Detector without contrast stretching. Only the brighter stars were detected and airplane streaks, but does not detect any of the SO edges.

and adaptive contrast stretching per zone (CSZ). The Raw case indicates that the I_{SN} was computed on an image with no image enhancement.

A second example of I_{SN} is shown in Fig. 10 at the bottom-left in which five rows are marked in the center part of image N° 13 of the dataset. Similarly to the previous case of Fig. 9, the upper-right of Fig. 10 shows the I_{SN} plot and the peak around pixel 18. The I_{SN} was also computed for different combinations of background subtraction (BS), image fusion (FU), star removal (SR), contrast stretching (CS), and adaptive contrast stretching per zone (CSZ). The Raw case indicates that the I_{SN} was computed in an image with no image enhancement. In this example, the SO is located in the periphery of the image. The bottom-right of Fig. 10 shows the $I_{SN} - \overline{I_{SN}}$ that allows a better

visualization of the improvements produced at different stages of the pipeline. The magnitude of the individual peaks of the I_{SN} and the $I_{SN} - \overline{I_{SN}}$ are maxima for the combination BS-FU-SR-CSZ, and coincide with the SO location. It is worth noting that because the SO in this case is fainter, and its shape is more irregular, it is more difficult to detect.

3.2. Results of the detection stage

3.2.1. Canny edges and progressive probabilistic Hough transform

The largest peaks of the I_{SN} and the $I_{SN} - \overline{I_{SN}}$ are obtained for the combination BS-FU-SR-CSZ. This shows the benefits of the proposed pipeline compared to the Raw case with no image enhancement. Figs. 11 and 12 show detection of SOs validated with the ground truth after applying the Canny method and the Progressive Probabilistic Hough Transform segment detector to the BS-FU-SR-CSZ image. The image enhancement per zones allows more uniform edge detection along the image, especially when there is an element with high brightness.

After proceeding with cross-validation, this methodology does not obtain great results, especially due false positives and low detection rates. Table 1 summarizes results of detection stage, showing Precision, Recall and f-score measurements.

3.2.2. Radon transform streak detection

The Radon Transform was applied to each zone, and streaks could be detected using the local maxima in the parameters space (sinogram). After that, the Inverse Radon Transform was applied to the local maxima and the streaks could be obtained. In the left part of Fig. 13
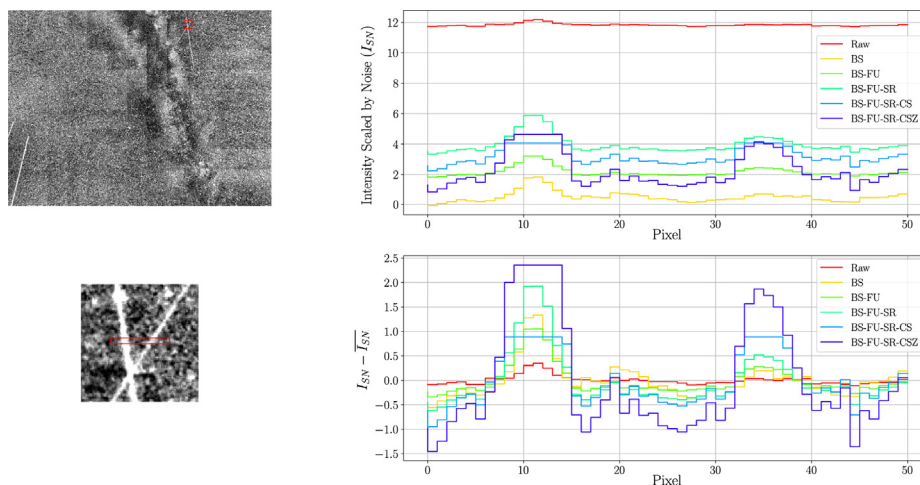

Fig. 9. (Left-top) Image of Fig. 7-right with the area to measure the I_{SN} and the $I_{SN} - \overline{I_{SN}}$ marked in red. (Left-bottom) Zoom on image left-top (Fig. 7-right), showing five randomly chosen rows to measure the I_{SN} and the $I_{SN} - \overline{I_{SN}}$. (Right-top) Shows the result of the I_{SN} and (Right-bottom) shows the result of the $I_{SN} - \overline{I_{SN}}$ computed on the five rows marked on left-bottom figure. The results show different combinations of preprocessing of the image including: background subtraction (BS), image fusion (FU), star removal (SR), contrast stretching (CS), and adaptive contrast stretching per zone (CSZ). The case, Raw, indicates no image enhancement was performed. (For interpretation of the references to colour in this figure legend, the reader is referred to the web version of this article.)
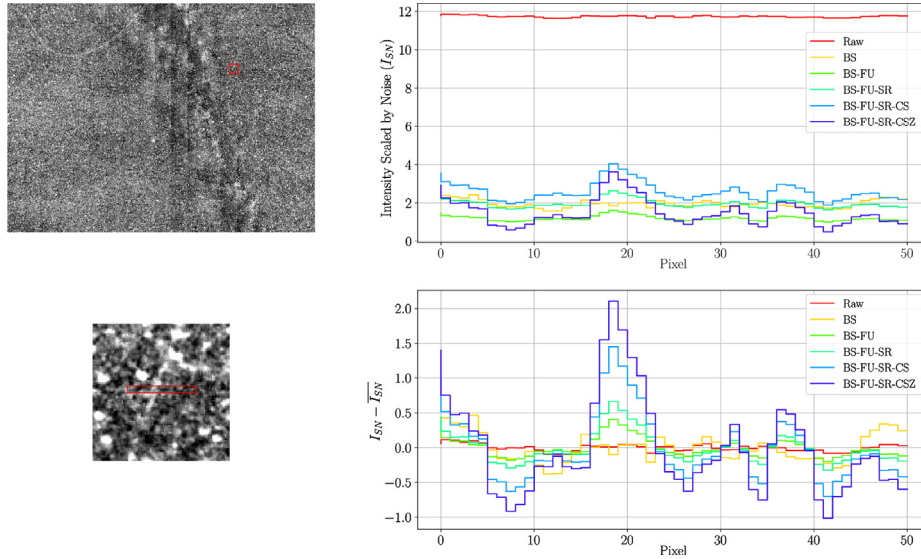
Fig. 10. (Left-top) Image N° 13 with the area of zoom marked in red. (Left-bottom) Zoom on the center part of image N° 13 of the dataset and processed with the pipeline, showing five randomly chosen rows to measure the I_{SN} and the $I_{SN} - \overline{I_{SN}}$. (Right-top) Shows the result of the I_{SN} and (Right-bottom) shows the result of the $I_{SN} - \overline{I_{SN}}$ computed on the five rows marked on left-bottom figure. The results show different combinations of preprocessing of the image including: background subtraction (BS), image fusion (FU), star removal (SR), contrast stretching (CS), and adaptive contrast stretching per zone (CSZ). The case, Raw, indicates no image enhancement was performed. (For interpretation of the references to colour in this figure legend, the reader is referred to the web version of this article.)
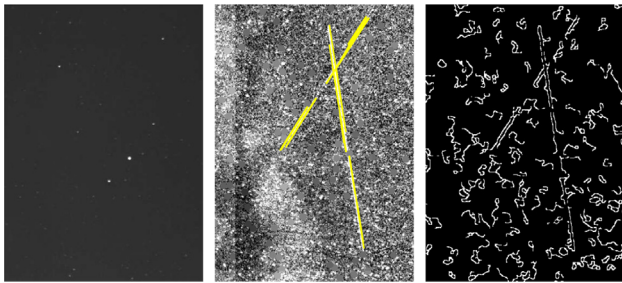

Fig. 11. Example of two positive SO detections. (Left) Original input image with SO. (Middle) Processed image with BS-FU-SR-CSZ. (Right) Canny edges.
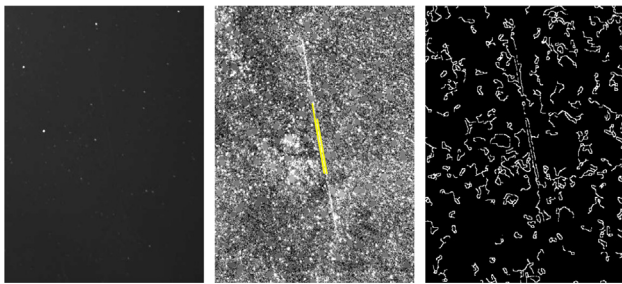

Fig. 12. Second example of SO detection (image N° 14, sensor 1 of dataset). (Left) Original input image with SO. (Middle) Processed image with BS-FU-SR-CSZ. (Right) Canny edges.

an input image zone is shown; in the middle of Fig. 13 the Randon Transform is shown, and the local maxima are marked. Finally, the right section of Fig. 13 shows the Inverse Radon Transform of the local maxima neighborhood that allows detecting the streaks correctly. Moreover,

Table 1
Detection measurements using both methodologies (Canny + Hough Transform and Radon Transform).

Method	Precision	Recall	f-score
Canny + PPHT	0.77 ± 0.028	0.69 ± 0.035	0.73 ± 0.026
Radon Transform	1.00 ± 0.000	0.94 ± 0.022	0.97 ± 0.012
RT without Fusion	1.00 ± 0.000	0.63 ± 0.038	0.77 ± 0.029

to avoid false positives, the local maxima must exceed a threshold (determined on the training images) defined by

$$T_R = \mu_S + C \cdot \sigma_S \qquad (4)$$

where μ_S is the sinogram's mean and σ_S is the sinogram's STD. The constant C was adjusted with a training image to each cross-validation fold.

After applying this methodology to all the zones, the SOs were detected and marked, as is shown in Fig. 14. Fainter streaks were detected using this approach as is shown in Fig. 15 an example of a detection of a very faint streak.

Using this methodology, the detection results improved with no false positives, as summarized in Table 1. It can be observed in Fig. 16 that the object not detected is very faint, difficult to identify by visual inspection, and it was located on the top border of the image. That is why it is not possible to obtain the necessary redundancy in the Radon Transform methodology.

3.3. Results without image fusion

To show the benefit of image fusion, we applied the pipeline without including the fusion step. Fig. 17-left
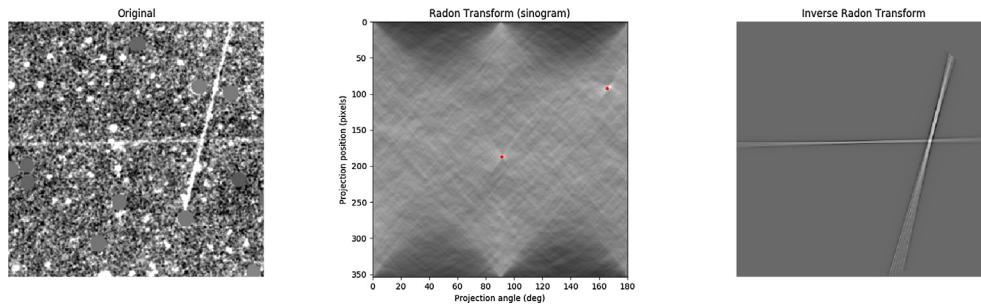
Fig. 13. Example of two positive SO detections using Radon Transform. (Left) Original input image with SO. (Middle) Randon Transform (sinogram). (Right) Inverse Radon Transform of peaks neighborhood.
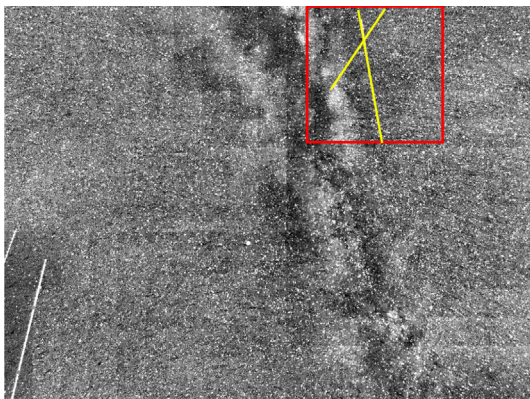

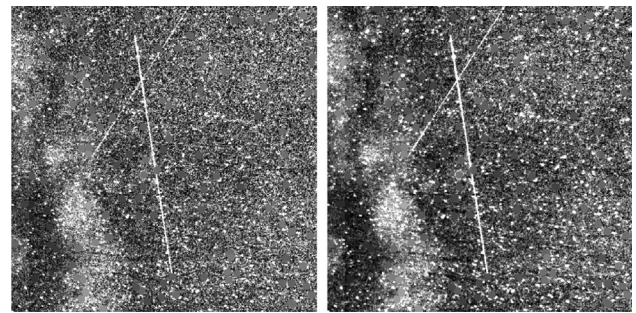Fig. 14. Example of results of Radon Transform methodology applied to whole image.

Fig. 17. Result of fusing the images from 3 sensors. (Left) Image from Camera 1, (Right) Fused Image using three Cameras.

objects, such as stars and SOs, were brighter and sharper. Also, some of the SOs were not visible without image fusion, as is shown in Fig. 18.

Results of computing the I_{SN}, and $I_{SN} - \overline{I_{SN}}$ for the fused image are shown in Fig. 19. It can be observed that the I_{SN} and the $I_{SN} - \overline{I_{SN}}$ improved in the case of SOs using the

shows the image from camera 1, and Fig. 17-right shows the fused image from the three sensors. It can be seen in the fused image that the noise was reduced while the
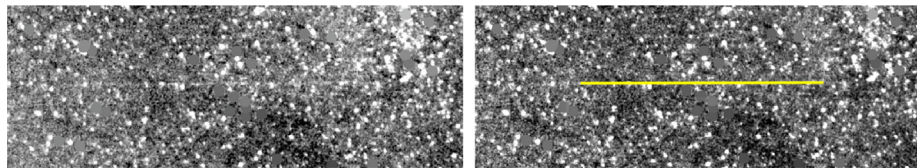

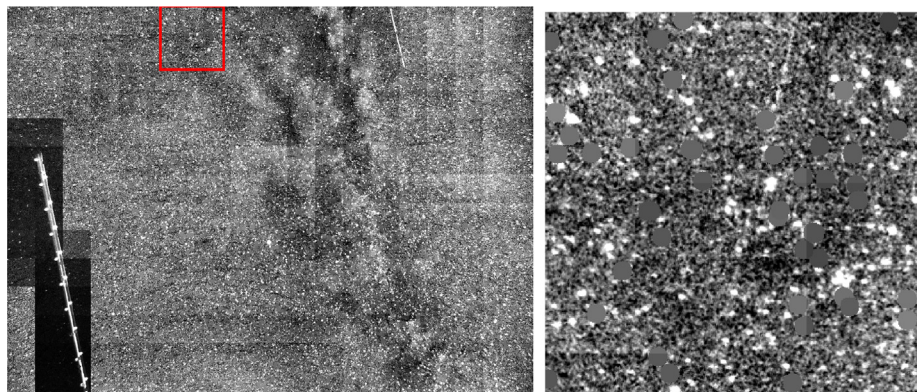Fig. 15. Very faint space object detected using Radon Transform methodology.

Fig. 16. False Negative SO (Left) Processed Image, (Right) Zoom in the area marked in red. (For interpretation of the references to colour in this figure legend, the reader is referred to the web version of this article.)
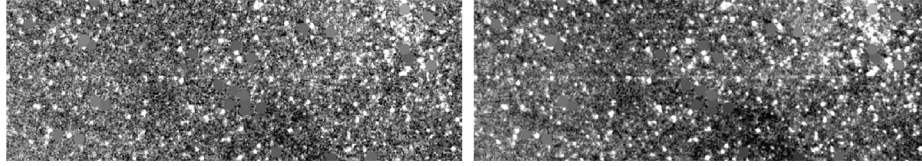
Fig. 18. Very faint Image of space object. (Left) Image from Camera 1, (Right) Fused Image using three cameras.
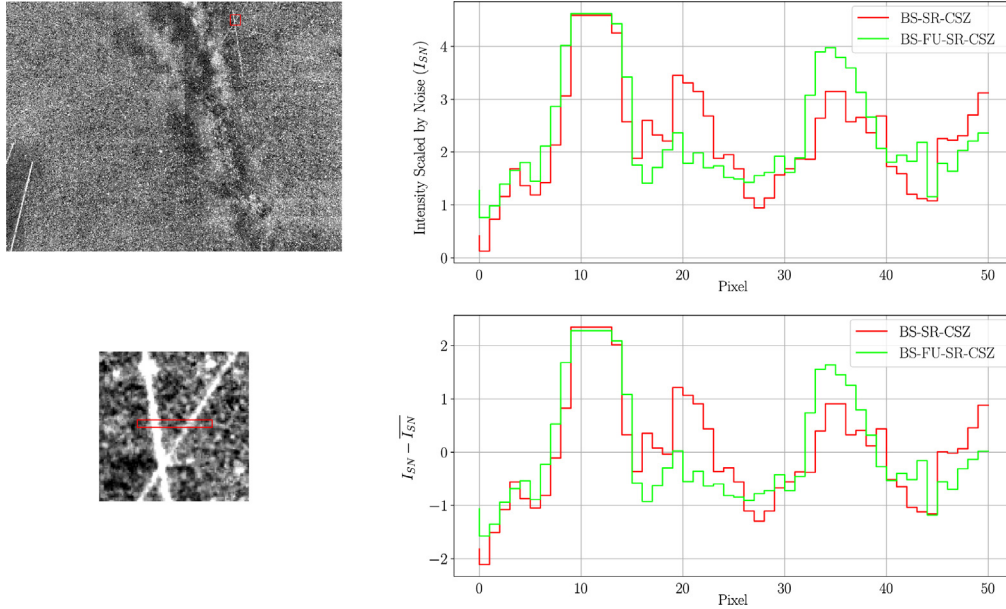

Fig. 19. (Top-left) Fusion of image N° 15 from the three sensors. The area of zoom is marked in red. (Bottom-left) Zoom on top-left image showing five randomly chosen rows to measure the I_{SN}, and the $I_{SN} - \overline{I_{SN}}$. The (Top-right) shows the result of the I_{SN} and (Bottom-right) shows the result of the $I_{SN} - \overline{I_{SN}}$ computed on the five rows marked on the bottom-left figure. (For interpretation of the references to colour in this figure legend, the reader is referred to the web version of this article.)

fused image compared to the I_{SN} and the $I_{SN} - \overline{I_{SN}}$ from only one image. The average ratio between the I_{SN} from the fused image and the Camera 1 image was 1.26 in the peaks for detected SOs, while, theoretically, the I_{SN} can improve by a factor of $\sqrt{3}$. Image registration and calibration errors conspire to reduce the effective improvement from fusing images. This effect can be observed in Fig. 19, where the streaks are wider, in addition to having larger I_{SN} values, and the I_{SN} values are lower in background zones.

Image fusion allows detection of SO that are not visible using only a single image. The Recall measurement decays using a single image, as can be observed in Table 1.

3.4. Streak detection results

Our method focuses on the accurate space object detection and in determining their trajectory. Due the fusion step of the three simultaneous captures, the streak visualization was significantly improved. We determined the time-stamping of the detected streaks and compared them to the ground-truth extracted from Space-Track.org with

NORAD ID as shown in Table 2. In average, the error among the detected streaks matching the length of the ground-truth was $0°38'$, while the position error was in average of $2°1'$, considering all detected streaks.

Comparing the results with and without image fusion, Table 3 shows how the estimated length of the streaks changed. This is significant especially in those cases where a faint streak was detected. The fusion improved the length detection. In average, the error of the detected streaks matching the length of the ground-truth was 4.84% ($0°54'$) without fusion, while this error was reduced to 3.45% ($0°38'$) with fusion.

Table 4 shows all streaks detected in the images with their respective NORAD ID. There are no new objects, but the positions were corrected respect to those of the catalog.

The contrast stretching step generates saturation in the pixel values and therefore the determination of the visual magnitude for the detected objects changes. Nevertheless, knowing the position and length of the detected objects, the visual magnitude can be obtained from the original image. Additionally, based on the magnitude of the stars present in the catalog and the area that each space object

Table 2
Space Objects coordinates extracted from Space-Track.org. Those coordinates were used as ground-truth. (–) means that this point is outside the FOV of the image.

NORAD ID	t_0	RA	DEC	t_f	RA	DEC
19650	01:23:16	–	–	01:23:46	298°12'	7°0'
19650	01:24:28	307°37'	22°22'	01:24:58	315°50'	32°50'
31211	01:24:28	265°10'	58°57'	01:24:58	–	–
28931	01:24:28	253°08'	31°12'	01:24:58	243°25'	46°43'
3598	01:24:28	234°19'	40°09'	01:24:58	253°22'	45°06'
3598	01:25:35	283°13'	46°01'	01:25:55	305°07'	41°34'
19650	01:25:35	327°44'	43°28'	01:25:55	–	–
18586	01:34:43	301°28'	10°27'	01:35:13	300°03'	24°30'
20663	01:40:52	267°40'	45°42'	01:41:22	282°34'	27°40'
33500	01:40:52	322°35'	49°31'	01:41:22	310°33'	34°59'
20663	01:41:57	293°38'	7°22'	01:42:27	–	–
33500	01:41:57	300°38'	15°20'	01:42:27	294°33'	−0°10'
9023	01:45:53	299°49'	4°29'	01:46:23	305°58'	17°06'
9023	01:45:53	320°31'	38°54'	01:46:23	331°41'	48°50'
27386	02:27:12	252°13'	49°53'	02:27:42	262°18'	37°24'

Table 3
Measured SO length on the ground-truth, with and without using the fusion step.

NORAD ID	Name	GT length	w/o fusion	w/ fusion
19650	SL-16 R/B	13°18'	12°44'	12°43'
28931	Alos	18°18'	18°15'	18°42'
3598	Atlas Centaur R/B	19°41'	17°34'	20°49'
3598	Atlas Centaur R/B	22°21'	20°16'	20°06'
18586	SL-8 R/B	14°07'	13°56'	14°09'
20663	Cosmos 2084	23°23'	22°00'	23°05'
33500	H-2A R/B	18°52'	19°45'	19°50'
33500	H-2A R/B	16°20'	15°18'	15°54'
9023	SL-8 R/B	14°02'	13°20'	13°38'
9023	SL-8 R/B	14°57'	15°29'	15°15'
27386	Envisat	16°03'	15°45'	16°17'

Table 4
Space Objects coordinates measured after applying our pipeline considering the fusion stage. (–) means that this point is outside the FOV of the image.

NORAD ID	t_0	RA	DEC	t_f	RA	DEC
19650	01:23:16	–	–	01:23:46	296°22'	7°20'
19650	01:24:28	304°58'	22°14'	01:24:58	312°09'	32°44'
31211	01:24:28	273°56'	48°28'	01:24:58	–	–
28931	01:24:28	253°25'	30°06'	01:24:58	243°42'	46°05'
3598	01:24:28	232°15'	40°04'	01:24:58	252°27'	45°07'
3598	01:25:35	281°36'	45°49'	01:25:55	301°20'	41°57'
19650	01:25:35	322°57'	43°29'	01:25:55	–	–
18586	01:34:43	300°38'	10°50'	01:35:13	298°39'	24°51'
20663	01:40:52	267°00'	46°17'	01:41:22	281°44'	28°31'
33500	01:40:52	324°41'	50°30'	01:41:22	311°21'	35°49'
20663	01:41:57	293°12'	8°43'	01:42:27	–	–
33500	01:41:57	300°49'	16°06'	01:42:27	294°35'	1°28'
9023	01:45:53	299°08'	4°22'	01:46:23	305°26'	16°28'
9023	01:45:53	321°05'	38°31'	01:46:23	332°46'	48°19'
27386	02:27:12	252°12'	49°37'	02:27:42	262°16'	36°49'

covers, the magnitude of these objects could be estimated by known methods such as differential photometry (Young et al., 1991; Robinson et al., 1995). It should be noted that due to the fusion step, the apparent magnitude of the objects increases.

4. Conclusions

Detection of SOs has many important applications, such as detecting debris that could become hazards for satellites or space missions in Low-Earth orbits. In this paper we

described a pipeline able to detect SOs automatically in images acquired with an all-sky camera and a large FoV. The pipeline is flexible in the sense that it is composed of several blocks that can be added or eliminated for image processing to improve the detection process.

The proposed pipeline includes the following main steps: image distortion correction, filtering for noise reduction, generation of a background model for subtraction, star elimination using a star catalog, local-based contrast enhancement, and, finally, for automatic SO detection, two methodologies were developed to detect line segments. The first one uses a Canny edge detector and a Progressive Probabilistic Hough Transform, while the second is based on the Radon Transform to detect line segments.

The method was applied to a dataset of 22×3 images obtained from the OmniSSA at the Georgia Institute of Technology. The OmniSSA has 3 sensors able to capture high-resolution images simultaneously (3352×2532 pixels) with wide FoV for each camera, and fusing images from those sensors improved the I_{SN} and the visualization during the detection stage.

A ground-truth was obtained from a well-known database and was marked in the images by human experts to validate the results of the pipeline considering information from the coordinates that were estimated using the results of Astrometry.net. Results showed that 15/16 SOs were correctly detected by the pipeline using the Radon Transform methodology.

Finally, the best results were obtained with the combination BS-FU-SR-CSZ for the image enhancement stage, and the Radon Transform methodology for the detection stage. For future work, parallelizing part of the code should improve computational times.

Acknowledgments

References

Blanton, M.R., Kazin, E., Muna, D., Weaver, B.A., Price-Whelan, A., 2011. Improved background subtraction for the sloan digital sky survey images. Astronom. J. 142 (1), 31.

Cament, L.A., Castillo, L.E., Perez, J.P., Galdames, F.J., Perez, C.A., 2014. Fusion of local normalization and gabor entropy weighted features for face identification. Pattern Recogn. 47 (2), 568–577.

Cament, L.A., Galdames, F.J., Bowyer, K.W., Perez, C.A., 2015. Face recognition under pose variation with local gabor features enhanced by active shape and statistical models. Pattern Recogn. 48 (11), 3371–3384.

Canny, J., 1986. A computational approach to edge detection. IEEE Trans. Pattern Anal. Mach. Intellig. 8 (6), 679–698.

Castillo, L., Cament, L., Galdames, F., Perez, C., 2014. Illumination normalisation method using kolmogorov-nagumo-based statistics for face recognition. Electron. Lett. 50 (13), 940–942.

Cheung, S.-C.S., Kamath, C., 2005. Robust background subtraction with foreground validation for urban traffic video. EURASIP J.Adv. Signal Process. 2005 (14), 726261.

Cucchiara, R., Grana, C., Piccardi, M., Prati, A., 2003. Detecting moving objects, ghosts, and shadows in video streams. IEEE Trans. Pattern Anal. Mach. Intellig. 25 (10), 1337–1342.

Fryer, J.G., Brown, D.C., 1986. Lens distortion for close-range photogrammetry. Photogramm. Eng. Remote Sens. 52 (1), 51–58.

Galamhos, C., Matas, J., Kittler, J., 1999. Progressive probabilistic hough transform for line detection. IEEE Computer Society Conference on omputer Vision and Pattern Recognition, 1999, vol. 1. IEEE, pp. 554–560.

Geisser, S., 2017. Predictive Inference. Routledge.

Grøtte, M., Virani, S., Holzinger, M., Register, A., Perez, C., Tapia, J., 2016. All-sky image fusion for a synoptic survey telescope in arctic and antarctic domains. In: Advanced Maui Optical and Space Surveillance Technologies Conference.

Gural, P.S., 2008. Algorithms and software for meteor detection. Earth Moon Planets 102 (1–4), 269–275.

Hartley, R., Zisserman, A., 2003. Multiple View Geometry in Computer Vision. Cambridge University Press.

Huang, T., Yang, G., Tang, G., 1979. A fast two-dimensional median filtering algorithm. IEEE Trans. Acoust. Speech Signal Process. 27 (1), 13–18.

Klinkrad, H., 2010. Space Debris. Wiley Online Library.

Krag, H., Serrano, M., Braun, V., Kuchynka, P., Catania, M., Siminski, J., Schimmerohn, M., Marc, X., Kuijper, D., Shurmer, I., et al., 2017. A 1 cm space debris impact onto the sentinel-1a solar array. Acta Astronaut. 137, 434–443.

Laas-Bourez, M., Blanchet, G., Boër, M., Ducrotté, E., Klotz, A., 2009. A new algorithm for optical observations of space debris with the tarot telescopes. Adv. Space Res. 44 (11), 1270–1278.

Landgraf, M., Jehn, R., Flury, W., Dikarev, V., 2004. Hazards by meteoroid impacts onto operational spacecraft. Adv. Space Res. 33 (9), 1507–1510.

Lang, D., Hogg, D.W., Mierle, K., Blanton, M., Roweis, S., 2010. Astrometry. net: Blind astrometric calibration of arbitrary astronomical images. Astronom. J. 139 (5), 1782.

Lim, J.S., 1990. Two-dimensional Signal and Image Processing. Prentice Hall, Englewood Cliffs, NJ, p. 710.

Mellinger, A., 2009. A color all-sky panorama image of the milky way. Publ. Astron. Soc. Pac. 121 (885), 1180.

Murphy, T.S., Holzinger, M.J., Flewelling, B., 2016. Space object detection in images using matched filter bank and bayesian update. J. Guid.Control Dyn. 40 (3), 497–509.

Olson, D.L., Delen, D., 2008. Advanced Data Mining Techniques. Springer Science & Business Media.

Pardini, C., Anselmo, L., 2011. Physical properties and long-term evolution of the debris clouds produced by two catastrophic collisions in earth orbit. Adv. Space Res. 48 (3), 557–569.

Perez, C., Castillo, L., Cament, L., Estevez, P., Held, C., 2010. Genetic optimisation of illumination compensation methods in cascade for face recognition. Electron. Lett. 46 (7), 498–500.

Perez, C.A., Cament, L.A., Castillo, L.E., 2011. Methodological improvement on local gabor face recognition based on feature selection and enhanced borda count. Pattern Recogn. 44 (4), 951–963.

Podbreznik, P., Potočnik, B., 2012. Assessing the influence of temperature variations on the geometrical properties of a low-cost calibrated camera system by using computer vision procedures. Mach. Vis. Appl. 23 (5), 953–966.

Radon, J., 1986. On the determination of functions from their integral values along certain manifolds. IEEE Trans. Med. Imaging 5 (4), 170–176.

Robinson, L., Wei, M., Borucki, W., Dunham, E., Ford, C., Granados, A., 1995. Test of ccd precision limits for differential photometry. Publ. Astron. Soc. Pac. 107 (717), 1094.

Tapia, J.E., Perez, C.A., Bowyer, K.W., 2016. Gender classification from the same iris code used for recognition. IEEE Trans. Inf. Forensics Secur. 11 (8), 1760–1770.

Torteeka, P., Gao, P.-Q., Shen, M., Guo, X.-Z., Yang, D.-T., Yu, H.-H., Zhou, W.-P., Zhao, Y., 2017. Space debris tracking based on fuzzy running gaussian average adaptive particle filter track-before-detect algorithm. Res. Astron. Astrophys. 17 (2), 18.

Trigo-Rodriguez, J.M., Madiedo, J.M., Gural, P.S., Castro-Tirado, A.J., Llorca, J., Fabregat, J., Vítek, S., Pujols, P., 2008. Determination of meteoroid orbits and spatial fluxes by using high-resolution all-sky ccd cameras. Earth Moon Planets 102 (1–4), 231–240.

Virtanen, J., Poikonen, J., Säntti, T., Komulainen, T., Torppa, J., Granvik, M., Muinonen, K., Pentikäinen, H., Martikainen, J., Näränen, J., et al., 2016. Streak detection and analysis pipeline for space-debris optical images. Adv. Space Res. 57 (8), 1607–1623.

Weryk, R., Brown, P., Domokos, A., Edwards, W., Krzeminski, Z., Nudds, S., Welch, D., 2008. The southern ontario all-sky meteor camera network. Earth Moon Planets 102 (1–4), 241–246.

Weryk, R., Campbell-Brown, M., Wiegert, P., Brown, P., Krzeminski, Z., Musci, R., 2013. The canadian automated meteor observatory (camo): system overview. Icarus 225 (1), 614–622.

Xie, X., Lam, K.-M., 2006. An efficient illumination normalization method for face recognition. Pattern Recogn. Lett. 27 (6), 609–617.

Young, A.T., Genet, R.M., Boyd, L.J., Borucki, W.J., Lockwood, G.W., Henry, G.W., Hall, D.S., Smith, D.P., Baliumas, S., Donahue, R., et al., 1991. Precise automatic differential stellar photometry. Publ. Astron. Soc. Pac. 103 (660), 221.

Zimmer, P., Ackermann, M., McGraw, J., 2013. Gpu-accelerated faint streak detection for uncued surveillance of leo. In: Advanced Maui Optical and Space Surveillance Technologies Conference.

Zimmer, P., McGraw, J.T., Ackermann, M.R., 2018. Real-time optical space situational awareness of low-earth orbit with small telescopes. In: Advanced Maui Optical and Space Surveillance Technologies Conference.